University of Bath

REVISION

18th May 2018

Contrasting Transient Photocurrent Characteristics for Thin Films of Vacuum-Doped "Grey" TiO₂ and "Grey" Nb₂O₅

**Moisés A. de Araújo [1,2], Murilo F. Gromboni [1], Frank Marken [2]*,
Stephen C. Parker [2], Laurence M. Peter [2], Josh Turner [3], Helen C. Aspinall [3],
Kate Black [3], and Lucia H. Mascaro [1]***

[1] *Department of Chemistry, Federal University of São Carlos, Rod. Washigton Luiz,
km235, CEP 13565-905, São Carlos, SP – Brazil*
[2] *Department of Chemistry, University of Bath, Claverton Down, Bath, BA2 7AY, UK*
[3] *School of Engineering, University of Liverpool, Liverpool L69 3GH, UK*

1

Abstract

Photo-catalytic performance for oxide films, here for inkjet-printed TiO_2 (ca. 1 μm thickness on FTO) and for spray-pyrolysis-coated Nb_2O_5 (ca. 1 μm thickness on FTO), is affected by oxygen vacancies that form during vacuum-heat treatment at 550 °C. The effects of the oxygen vacancies are associated with formation of Ti(III) and Nb(IV) sites, respectively, and therefore optically visible as "grey" coloration. Photo-electrochemical light-on-off transient experiments are performed in the limit of thin film photoanodes, where front and back illumination result in the same photo-current responses (*i.e.* with negligible effects from internal light absorption gradients). It is shown that generally the magnitude of photo-currents correlates linearly with light intensity, which is indicative of dominant "photo-capacitive" behaviour. At an applied voltage of 0.4 V vs. SCE (in the plateau region of the photo-current responses) the potential and also the pH (going from 1.0 M KOH to 0.1 M $HClO_4$ in the presence of methanol quencher) have no significant effect on photo-currents; that is, surface chemical/kinetic effects appear to be unimportant and interfacial hole transfer may be rate limiting. Under these conditions (and based on a simplistic mechanistic model) changes in photo-currents introduced by oxygen vacancy doping (detrimental for TiO_2 and beneficial for Nb_2O_5) are assigned primarily to changes in electron mobility.
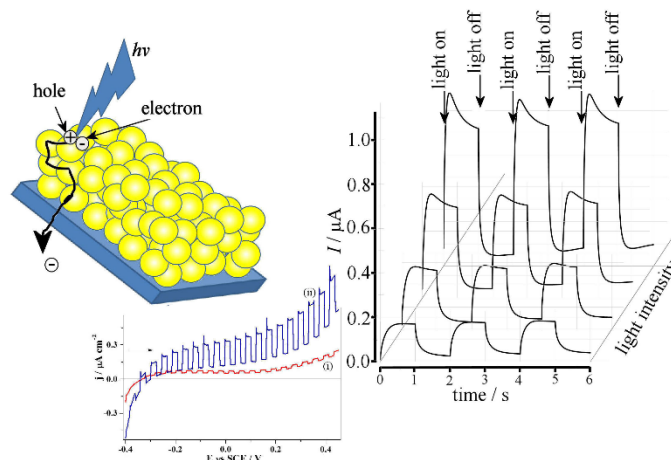
Graphical Abstract

Keywords: photosynthesis; water splitting; thin film oxide; digital simulation; transient

1. Introduction

Semiconductor film electrodes, usually poly-crystalline and mesoporous, are now commonly employed in photo-electrochemical devices such as photovoltaic cells [1], photogalvanic cells [2,3], in solar water splitting [4], artificial solar electrosynthesis [5], or in solar carbon dioxide reduction [6]. Many new types of materials [7] and architectures [8] have been developed to enhance performance, provide better sustainability [9], or to lower costs. Methods to further tailor semiconductor performance include chemically embedding dopants [10,11], physical doping (for example by hydrogen treatment [12], plasma treatment [13], or by vacuum annealing [14]), surface modifications [15,16], crystal orientation [17,18,19,20] and crystal engineering [21], or layering of materials [22]. Some materials such as TiO_2 (as originally proposed by Honda [23]) remain highly interesting and subject to intense study, whilst other systems such as Nb_2O_5 (initially studied by Diquarto [24]) provide more niche solutions, based for example on the natural availability of niobia in particular in mines in Brazil [25]. Further study of these materials is often driven by the need to better unravel the complex link between electronic/structural

properties, mechanism, and photo-electrochemical performance. Here, a mechanistic analysis is attempted (in the limit of very thin films) for contrasting the behaviour of thin films of TiO_2 and Nb_2O_5 before and after vacuum doping.

Multiple factors affect photo-reactivity of mesoporous oxide films of which electron (or hole) mobility and rates of recombination/chemical processes are particularly crucial. The associated rate constants for these processes are usually assumed "ideal"; but in reality they may depend on location in the bulk or at a surface, on direction of transport within crystal domains, dispersion of properties, or on particular surface facets or sites. In a very oversimplified manner (and avoiding the classical band model for bulk semiconductors [26]), for a thin film of nano-material of thickness δ_{film} (assuming fully shielded conditions – pores flooded with electrolyte [27] – so that effects of migration and potential gradients can be ignored), it is possible to approximately express the transport layer for electrons reaching the substrate|oxide interface, $\delta_{transport,e} = \sqrt{2D_e t}$, and for holes reaching the oxide|aqueous electrolyte interface, $\delta_{transport,h} = \sqrt{2D_h t}$ [28]. Reaction layer dimensions can be assigned based on reaction of holes with first order rate constant k_c (for oxygen evolution) at the surface, $\delta_{reaction,h} = \sqrt{D_h/k_c}$, and based on electrons recombining with holes via second order kinetics, $\delta_{recombination,e} = \sqrt{D_e/k_{rec}n_h}$ (often assumed is a low steady state concentration n_h to give pseudo-first order). However, the relative relevance of these parameters in the overall mechanism is not immediately apparent and needs further investigation in the context of a simplified model. Figure 1 shows a cartoon with some light-on and light-off transient processes (others are possible) leading to either hole or electron concentration build-up in the film (*vide infra*).
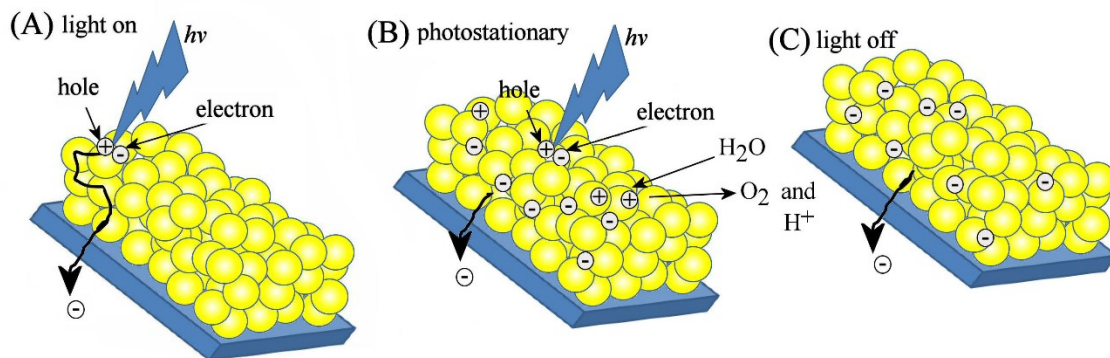
Figure 1. Schematic drawing of the formation of holes and electrons upon photo-excitation of thin film oxides on an electrically conducting substrate. (A) Light-on process with electrons being more mobile leading to some capacitive charging. (B) Photo-stationary state limited by the surface reaction and oxygen evolution. A positive net charge layer develops close to the substrate and a negative net charge layer develops close to the solution phase. (C) Light-off transient based on residual charge carriers being collected at the substrate.

Due to the second order nature of the recombination process, hole and electron concentrations are coupled, and this can lead to complexity in concentration profile changes for holes and electrons during light-on and light-off transients. Doping is often reported to affect D_e (due to a change in electron mobility), k_{rec} (due to additional recombination sites), and/or k_c (due to changes in surface states), but in reality other additional parameters/effects may also have to be taken into account. Currently there are very limited diagnostic tools or criteria available. This study introduces light intensity as diagnostic tool and re-considers some of the effects of doping induced by vacuum annealing for thin oxide films. It attempts a qualitative analysis based on both, photo-current transient shape and light intensity effects. Oxygen vacancy doping *via* vacuum annealing is considered for two types of oxide thin films: ink-jet printed titania (TiO_2) and

5

spray-pyrolysis-coated niobia (Nb_2O_5), both annealed in air at 550 ºC and then treated via vacuum annealing at 550 ºC.

Vacuum annealing is known to cause significant changes in reactivity, for example in hematite films [29], and has been employed for enhancing conductivity and/or photo-electrochemical performance in many oxide materials [30,31]. The effects are due to oxygen removal from the solid state crystal lattice associated with defect states. For titania, TiO_2, (and in particular for anatase, which has been extensively studied as semiconductor material [32]) oxygen vacancy doping has been induced by reducing conditions [33]. The formation of "black" or reduced TiO_2 has been reported for example after treatment with aluminium [34], magnesium [35], hydrogen [36], borohydride [37], by annealing in inert atmosphere [38], or *via* laser treatment in water [39]. Black titania has recently been reported to allow photochemical conversion of CO_2 to methane [40]. The surface of titania is reported to become more catalytically active [41], but bulk conductivity also is affected [42,43]. Also "grey" titania has been reported to perform well under photo-catalytic conditions [44].

Niobia, Nb_2O_5, represents one of an extended family of niobium oxide materials and phases [45]. The chemical [46] and (photo-)electrochemical properties [47,48] of Nb_2O_5 have been reported. Nb_2O_5 can be prepared *via* soft chemical routes [49] and has been employed for example in switchable photo-chromic windows [50]. Carbon-doped niobia with improved photocatalytic activity was obtained with a flame-pyrolysis approach [51]. The observation of "black" Nb_2O_5 with improved photo-electrochemical water splitting performance was

reported for example by Cui and coworkers [52]. Black niobia is obtained with aluminum as the reducing agent [53], the reduction of Nb_2O_5 associated with increased electrical conductivity has been observed after heating in hydrogen atmosphere [54], and also thermal vacuum-annealing has been reported to convert Nb(V) to Nb(IV) [55]. It seems plausible that similar effects are important for both TiO_2 and for Nb_2O_5 when oxygen vacancies are generated.

One way to introduce oxygen vacancies and thereby to condition or modify thin semiconductor films based on oxides is vacuum annealing. This method combines thermal activation of defect mobility with lower oxygen partial pressure to extract oxygen from the surface of the oxide material. As a result, pairs of defects are formed at the surface, which then diffuse into the oxide material to provide dopant/defect sites. In particular for TiO_2 this is well-documented, and it has been shown to result first in beneficial effects on photo-activity (at moderate doping level) and second in detrimental effects due to over-doping [56]. The two counter-acting phenomena most often discussed within the context of oxygen vacancy doping are improved electron conductivity and enhanced recombination. In this report the behaviour of two types of thin oxide films are contrasted before and after vacuum-annealing: TiO_2 and Nb_2O_5. It is suggested that changes in electron conductivity are primarily responsible for changes in photo-currents. With the help of an electron/hole diffusion model the importance of other reaction parameters (such as hole mobility) in limiting the maximum photo-current is investigated.

2. Experimental

2.1. Chemical Reagents

Chemical reagents were of analytical grade, and were used directly without further purification: ammonium niobate(V)oxalate hydrate, $C_4H_4NNbO_9 \cdot x\ H_2O$ (Sigma-Aldrich, 99.99%); Brij® O10, $C_{18}H_{35}(OCH_2CH_2)_nOH$ (Sigma-Aldrich); KOH (Sigma-Aldrich, 85%); perchloric acid, $HClO_4$ (Sigma-Aldrich, 70%); methanol, CH_3OH, (Sigma-Aldrich, 99.8%); Ti(IV)(isopropoxide)$_4$ (97%, Sigma-Aldrich); dimethoxyethane (anhydrous, 99.7%, Sigma-Aldrich).

2.2. Electrochemical Measurements

For electrochemical measurements an Autolab PGSTAT30 system was employed in three-electrode configuration with platinum wire counter electrode and KCl-saturated calomel (SCE) reference electrode. Photo-electrochemical measurements were performed in an electrochemical cell. The working electrode was either white or grey TiO_2 or Nb_2O_5 deposited on fluorine-doped tin oxide (FTO) substrates. The electrolyte was either 1.0 mol L^{-1} KOH pH 13.74, or 1.0 mol L^{-1} KOH with 0.5 mol L^{-1} CH_3OH, or 1.0 mol L^{-1} CH_3OH in 0.1 mol L^{-1} $HClO_4$. The electrodes were back-side or front-side illuminated with LEDs (Thorlabs, UK) as a function of intensity and at two different wave lengths, 385 and 450 nm.

2.3. Procedures

White and Grey TiO₂ Film Preparation. In order to deposit TiO_2 on a FTO substrate (obtained from Image Optics Components, Basildon, UK) by a piezoelectric inkjet printer, a Microfab Jetlab 4 was used at room temperature under ambient atmosphere with a 50 μm diameter nozzle. Printing was conducted using an applied voltage of 35 V, with a 36 μs pulse width and a frequency of 500 Hz. A drop spacing of 0.1 mm was used for all TiO_2 inks, with a print speed of 6 mmps. A TiO_2 ink containing the following composition was initially prepared: 0.15 cm^3 of Ti(IV)isopropoxide and 0.25 cm^3 dimethoxyethane in 4.6 cm^3 isopropanol resulting in an ink of 0.1 M Ti(IV)isopropoxide with 5 eq. dimethoxyethane in an isopropanol carrier vehicle. The photo-anodes printed containing 10 passes (printed in 10 layers) were annealed in air at 550 °C for 3 h, and another set were annealed under vacuum at 550 °C for 3 h. TiO_2 films were obtained with typically 1 μm thickness (Figure 2A-C).

White and Grey Nb₂O₅ Film Preparation. Ammonium niobate(V)oxalate hydrate (1.0 g) was dissolved in a mixture containing 1 cm^3 of Brij® O10 dissolved in 10 cm^3 of deionized water. The resulting mixture was stirred for 30 min, and then used to obtain Nb_2O_5 films by spray pyrolysis. A sprayer (compressed air driven, Gocheer 100-250 V dual action airbrush) with the head nozzle at a height of 9 cm from the substrate was used to spray nearly for 1 second onto a FTO substrate, which was on a hotplate at 160 °C. Solvent was allowed to evaporate for 30 seconds. In order to increase the thickness, this procedure was repeated. Subsequently the films were annealed in air at 550 °C for 3 h, and

treated in vacuum at 550 °C for 3 h. Nb_2O_5 films were obtained with typically 1 μm thickness (Figure 2D-F).

Digital Simulation. In order to explore charge diffusion during light-on and light-off transients, a Fortran programme was written and executed on a Vostro PC with 64-bit operating system and 3 GHz processor in Mathlab R2017b environment.
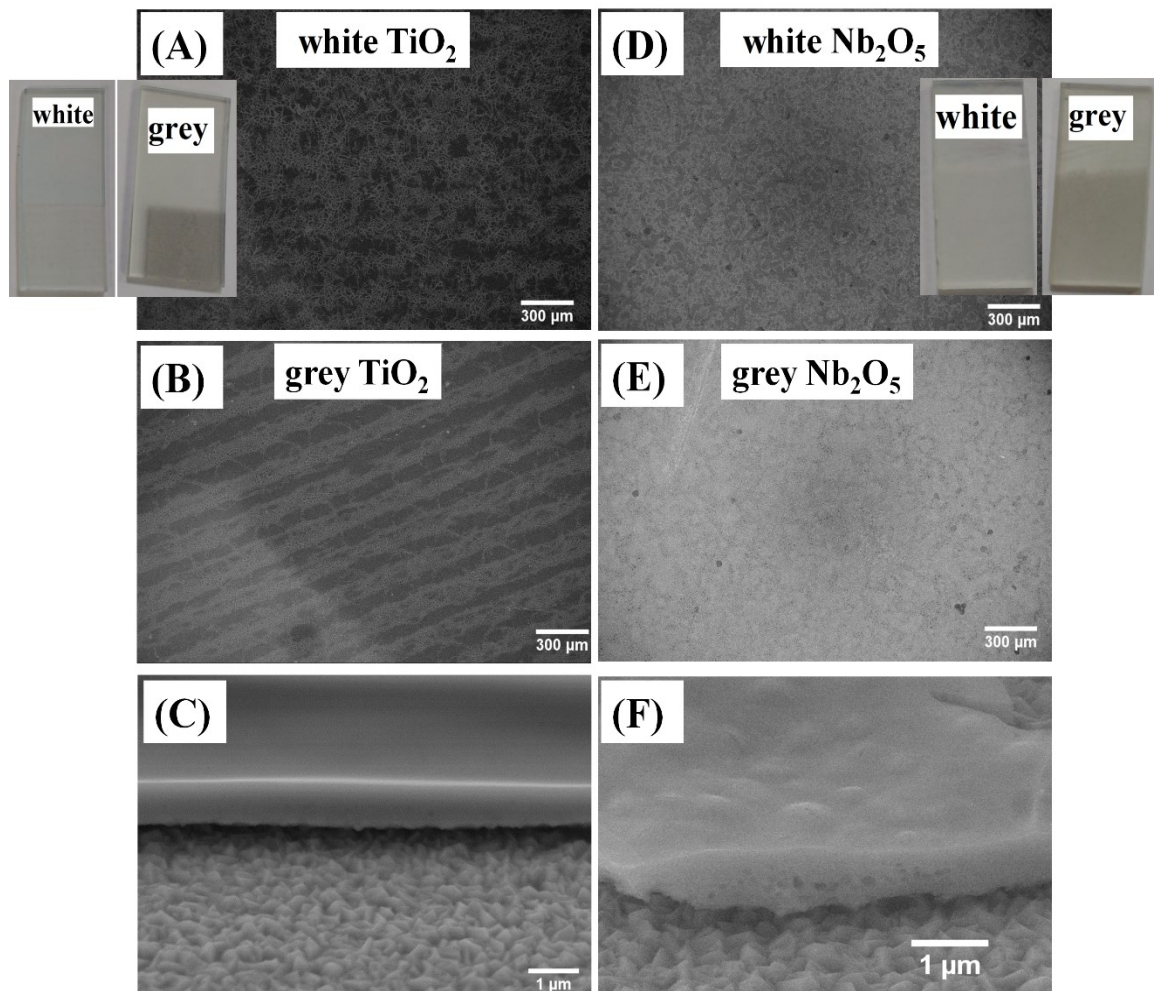

Figure 2. Scanning electron microscopy (SEM) images for (A,B,C) white and grey TiO_2 and (D,E,F) white and grey Nb_2O_5. Insets show optical photographs of thin films on FTO substrates.

Characterization of White and Grey TiO$_2$ and Nb$_2$O$_5$ Films. X-ray diffraction (XRD) data for both materials were obtained on a Rigaku DMax 2500PC X-ray diffractometer with CuKα wave length radiation of 1.54 Å, which was produced at an accelerating voltage of 40 kV and with a beam current of 150 mA. The 2θ range scanning was from 5 to 110° at a scanning rate of 1° s^{-1}, and at a step of 0.02°. Phase identification was carried out using the Crystallographica Search-Match Version 2.1.1.1 software. The microstructure analyses for both materials were also conducted with a Raman spectrometer Bruker Senterra using a laser with a wavelength of 532 nm and a power of 5 mW. Each spectrum was obtained in a range from 50 to 1540 cm^{-1} and a spectral resolution of 3-5 cm^{-1}. The scanning electron microscopy (SEM) images were obtained on a Zeiss-Supra 35, which was applied to investigate the morphology and the topology of the films. To estimate the optical band gap of the materials, UV-Vis spectra were recorded using a Varian Cary 5G UV-Vis-NIR spectrometer at the diffuse reflectance mode.

3. Qualitative Theory

Although partial analytical solutions for limiting cases of the complex mechanism for photo transients in thin film oxides have been proposed, there are many inter-dependent parameters to explore. Therefore, simplifying assumptions are commonly introduced, such as treating recombination as pseudo-first order process. Here, a simplistic digital simulation approach is employed (assuming diffusion and reaction of holes and electrons as chemical species and not considering different electron or hole energies) to maintain some of the complexity (*e.g.* the second order nature of recombination and geometry effects on

recombination) of the multi-parameter analysis and to develop a better (at least qualitative) picture of processes and of concentration gradients within thin mesoporous oxide films under illumination. Approaches to transient shape analysis for photo-transients have been previously developed, for example by Peter and coworkers [57] and can be based on two fundamental continuity equations (equation 1 and 2) with terms for light absorption, diffusion of electrons and holes, a second order recombination term, and a chemical term for a first order reaction consuming holes.

$$\frac{\partial n_e}{\partial t} = aI_0 + D_e \frac{\partial^2 n_e}{\partial x^2} - k_{rec} n_e n_h \tag{1}$$

$$\frac{\partial n_h}{\partial t} = aI_0 + D_h \frac{\partial^2 n_h}{\partial x^2} - k_{rec} n_e n_h - k_c n_h \tag{2}$$

In these equations the concentrations of holes and electrons, n_h and n_e (in mol m^{-3}), are linked to the extinction coefficient α (in m^{-1}; the inverse of the penetration depth), the light intensity I_0 (in mol m^{-2} s^{-1}), the diffusion coefficients D_e and D_h (in m^2 s^{-1}), the rate constant for recombination k_{rec} (in mol^{-1}m^{3}s^{-1}), and the rate constant for the chemical reaction of holes, k_c (in s^{-1}). Although some of these processes are clearly heterogeneous, the model assumes fully shielded and quasi-homogeneous conditions (based on the small size of individual nanoparticles) to give average concentration profile information. This model still leads to considerable complexity, and therefore the diffusion coefficients are fixed (here D_e = 10^{-13} m^{2}s^{-1} and D_h = 10^{-19} m^{2}s^{-1}; the considerable difference in diffusion coefficients for electrons and holes is assumed to be in part linked to differences in lattice reorganization energies) so that significant currents are produced only by electron diffusion. The mobility of holes is intentionally chosen so low that direct effects from holes

on the current response are here eliminated. Holes are likely to be driven (by dielectric stabilization) over short distances to the oxide | aqueous surface. Their life time is linked to the k_{rec} parameter. The interfacial flux $D\frac{\partial n_e}{\partial x}$ at the boundary of substrate electrode to oxide film multiplied by F (the Faraday constant) and A (the area) is employed to express the current [58].
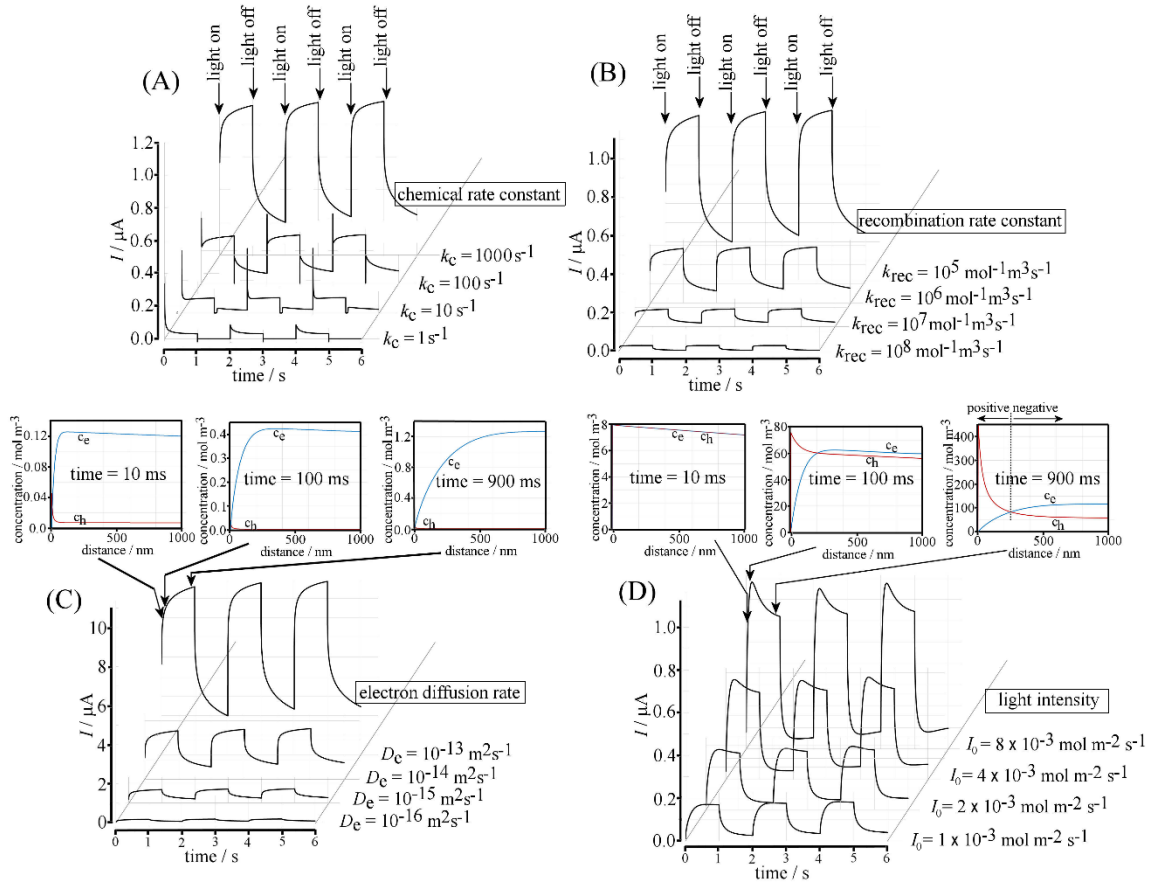

Figure 3. Data from digital simulation for three consecutive light-on-off photo transients for $D_e = 10^{-13}$ m^{2}s^{-1}, $D_h = 10^{-19}$ m^{2}s^{-1}, $I_0 = 10^{-3}$ mol m^{-2}s^{-1}, $\alpha = 10^5$ m^{-1} and (A) $k_{rec} = 10^5$ mol^{-1}m^{3}s^{-1}, varying k_c; (B) $k_c = 10^3$ s^{-1}, varying k_{rec}; (C) $k_c = 10^3$ s^{-1}, $k_{rec} = 10^2$ mol^{-1}m^{3}s^{-1}, varying D_e (insets showing concentration profiles); (D) $k_c = 1$ s^{-1}, $k_{rec} = 10^{-4}$ mol^{-1}m^{3}s^{-1}, varying I_0 (insets showing concentration profiles). A switch from positive to negative net charge is indicated.

13

When performing digital simulation "experiments" the parameter space can be explored and individual components investigated. Figure 3 shows a data summary for this exploration. Some insights from the model calculations can be expressed as follows:

- When investigating the concentration of holes and electrons in the illuminated film electrode material <u>far away from the substrate</u> and without chemical reaction ($k_c = 0$ s^{-1}), the initially generated concentration of holes and electrons is equal throughout and given by $I_0\,\alpha = k_{rec}\,n_e\,n_h$ or $n_e = n_h = \sqrt{\dfrac{I_0\,\alpha}{k_{rec}}}$. There is no net charge generated. However, with holes reacting chemically ($k_c > 0$ s^{-1}), a net negative charge builds up with time (excess of electrons) and the electron concentration increases to $n_e = \dfrac{I_0\alpha}{k_{rec}n_h}$ as the hole concentration converges towards zero. <u>Closer to the substrate electrode</u>, electrons are extracted and n_h increases giving locally a net positive charge (excess of holes).

- When inhibiting the chemical reaction ($k_c = 0$), a transient current response is generated with decaying current characteristics (see Figure 3A). This is associated with electrons transferring into the substrate electrode and holes remaining in the film (photo-capacitive charging). Analysis of this current transient suggests at least initially Cottrellian characteristics. A net positive charging effect of the oxide film occurs (assuming no other contributions to the charge) and the transient can be understood as dominated by "photo-capacitance".

- When increasing the chemical reaction rate (from $k_c = 1$ s^{-1} to 10 s^{-1}), a new secondary transient appears (see Figure 3A). The initial decaying transient is now complemented by the secondary rising transient. This rising transient is associated with "photo-reaction" of holes and therefore associated with a build-up of negative charges in most of the oxide film electrode. A plateau current is reached that increases with k_c. The switch from "photo-capacitance" to "photo-reaction" transient can be expressed (for very thin films) as the point of the apparent reaction layer equaling the film thickness, $\delta_{reaction,e} = \delta_{film}$ or $k_c = \frac{D_e}{\delta_{film}{}^2}$. That is, k_c needs to be fast enough for the photo-reaction to be observed in the current transient.

- Data in Figure 3B show the effect of the recombination rate constant k_{rec} on the photo-transient currents. Obviously the photo-currents increase with less recombination and this is linked to the build-up of a higher concentration n_e. In first approximation the magnitude of the current scales with hole concentration $\sim \sqrt{\frac{1}{k_{rec}}}$ as suggested above.

- Figure 3C shows data for "photo-reaction" transients as a function of electron diffusion coefficient, D_e. Also shown are concentration profile plots for holes and electrons at time 10 ms, 100 ms, and 900 ms. It can be seen that with time the hole concentration decreases as the electron concentration increases (due to the reaction of holes with $k_c = 1000$ s^{-1}). The rise in n_e is accompanied by the rise in photo-current up to a plateau. If all the absorbed photons generate electrons, this can be expressed as $\delta_{film} \alpha I_0 = \frac{D_e n_e}{\delta_{film}}$ to give a limiting concentration of $n_e =$

15

$\frac{\alpha I_0 \delta_{film}^2}{D_e}$ similar to that observed at 900 ms. For the "photo-reaction" case, this causes the plateau current to increase with approximately $\sqrt{D_e}$ dependency rather than linear with D_e.

- Figure 3D demonstrates the effect of varying the light intensity I_0. In the case of a higher chemical rate constant, $k_c = 1000$ s^{-1} (the "photo-reaction" case; not shown), the photo-current is predicted to increase proportional to $\sqrt{I_0}$ due to both n_h deceasing and n_e increasing simultaneously in the photo-reactive transient. However, for data in Figure 3D with $k_c = 1$ s^{-1}, the photo-capacitance case is dominant and the plateau current increases approximately linear with I_0. Note the region of net positive (close to the substrate electrode) and net negative charge (close to the solution phase) predicted within the oxide film. Based on this analysis of photo-transient data, it is therefore helpful to use the light intensity as diagnostic tool and to distinguish between "photo-capacitive" (decaying) and "photo-reactive" (rising) transients.

4. Results and Discussion

4.1. Characterization of Thin Films of White and Grey TiO$_2$ and Nb$_2$O$_5$

Films of TiO$_2$ or Nb$_2$O$_5$ were formed with a thickness of typically 1000 nm (see Figure 2) on fluorine-doped tin oxide (FTO) substrates. These films were initially produced at 550 ^{o}C in air to give white deposits. A post-treatment at 550 ^{o}C under vacuum conditions (oil-pump vacuum ca. 0.1 Torr) then caused a grey coloration to appear (see Figure 2 insets). Figure 4 shows XRD data for both TiO$_2$ and Nb$_2$O$_5$ before and after vacuum annealing

treatment. A significant change is observed for the TiO_2 peak 25.5° (consistent with the (101) peak in anatase indexed as in PDF n° 21-1272 [59]), which broadens upon vacuum annealing. The diffraction pattern for Nb_2O_5 (consistent with T-Nb_2O_5 orthorhombic phase and indexed according to PDF n° 28-317 [60]). However, these XRD data are not sufficiently clear to rule out other Nb_2O_5 phases with similar diffraction pattern [45,51]. There is no significant change before and after vacuum annealing.
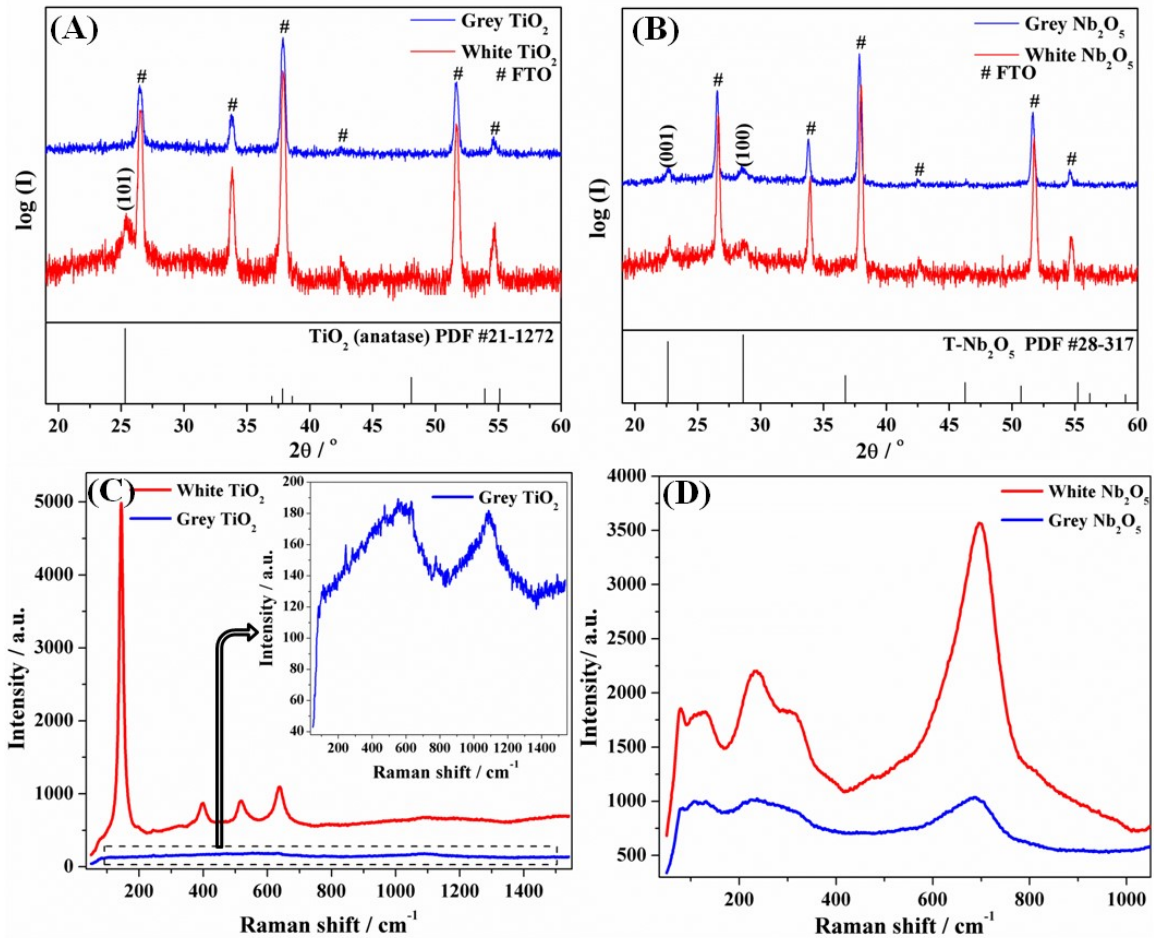

Figure 4. (A) XRD data for white TiO_2 and grey TiO_2. (B) XRD data for white and grey Nb_2O_5. (C) Raman spectra for white and grey TiO_2. (D) Raman spectra for white and grey Nb_2O_5.

In order to further confirm the microstructure of both materials and changes after vacuum treatment, Raman scattering was carried out and data are presented in Figures 4C and 4D for both TiO_2 and Nb_2O_5, respectively, before and after vacuum annealing treatment. The Raman spectra in Figure 4C present five Raman active modes for the white TiO_2 anatase phase, which were detected at 144 cm^{-1} (E_g), 199 cm^{-1} (E_g), 399 cm^{-1} (B_{1g}), 517 cm^{-1} (A_{1g}) and 640 cm^{-1} (E_g) [61]. The most intense band at 144 cm^{-1} was assigned to the external vibration of the Ti-O bond [60]. For the TiO_2 film vacuum annealing treatment resulted in broadening and blue shifts to 549 and 1080 cm^{-1} compared to the original TiO_2 bands at 517 and 640 cm^{-1}. The blue shift and broadening for the grey film may be due to the presence of defects, which are correlated to an increase amount of oxygen vacancies [60]. The Raman spectrum for the grey TiO_2 also indicates that the band at 144 cm^{-1} has dramatically decreased intensity. Tian and coworkers [62] reported the same phenomenon for the black TiO_2 materials obtained at different temperatures. Such behaviour was ascribed to the higher electronic conductivity, which would result in a shallower skin depth for the incident photons causing lower Raman scattering intensity.

The Raman spectrum for the white $T-Nb_2O_5$ is depicted in Figure 4D. The bands detected were located at 123 cm^{-1}, which is attributed to the lattice vibration mode of $T-Nb_2O_5$, 236 cm^{-1} (T_{2u}), 305 cm^{-1} (T_{2u}), 698 cm^{-1} (TO) and 814 cm^{-1} (TO) [51]. The strongest band at 698 cm^{-1} is attributed to the bond order of the niobia polyhedral and structure order [51]. The Raman spectrum for the grey Nb_2O_5 in Figure 4D shows broadening of all bands, indicating possibly a decrease of bond order and a more disordered structure, which is

18

associated to the increase of amount of oxygen vacancies [51]. Regarding the optical properties for both white and grey TiO_2 and Nb_2O_5, the Tauc plots were obtained and are depicted in Figure 5. The optical E_g values for both materials estimated from data in Figure 5 are presented in Tables 1A and 1B.
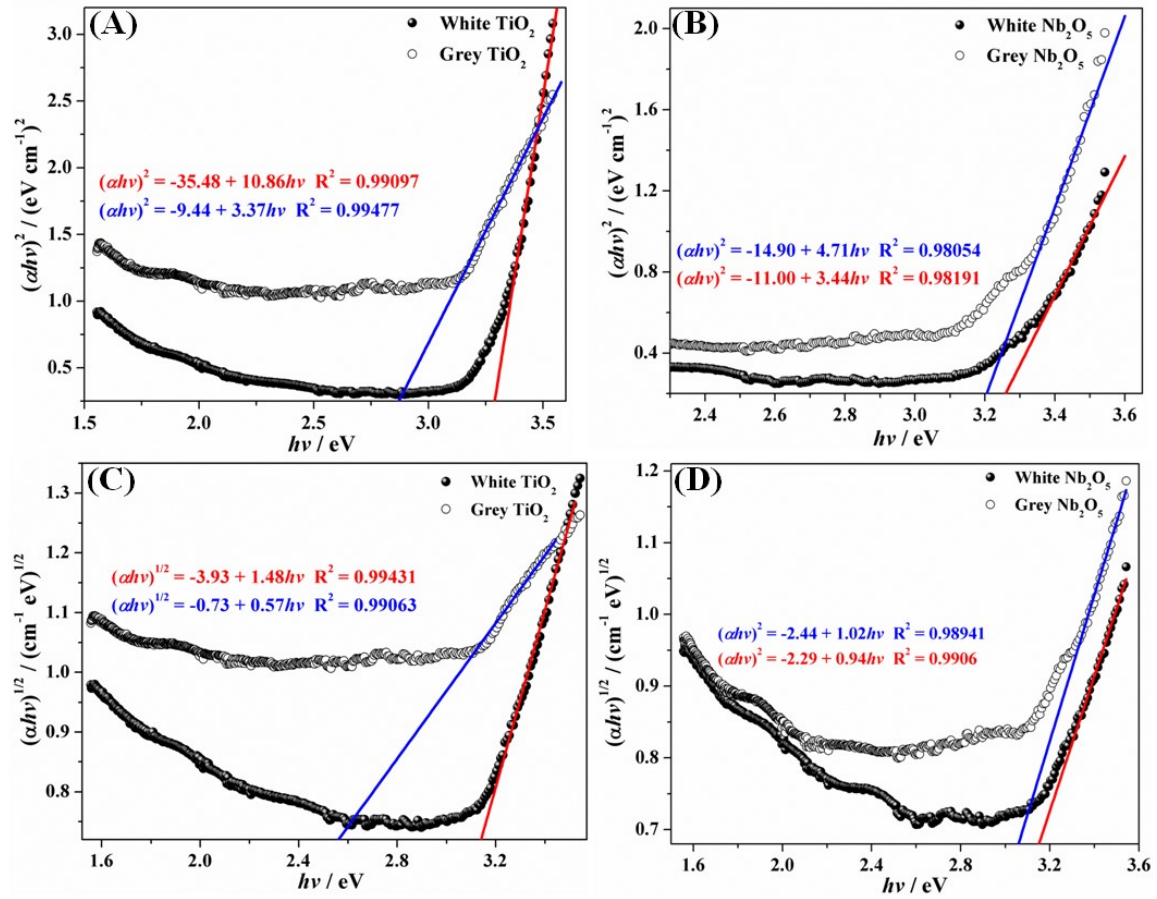

Figure 5. (A,B) Tauc plots comparing white and grey TiO_2 and Nb_2O_5, respectively, for a direct (allowed) transition. (C,D) Tauc plot comparing white and grey TiO_2 and Nb_2O_5, respectively, for an indirect (allowed) transition.

Table 1A. Summary of data from Tauc plots (Figure 5) of white and grey TiO_2.

Material	E_g / eV (nm)	E_g / eV (nm)
White TiO_2	3.27 (379)	2.67 (464)
Grey TiO_2	2.80 (442)	1.28 (969)
Type of transition	direct (allowed)	indirect (allowed)

Table 1B. Summary of data from Tauc plots (Figure 5) of white and grey Nb_2O_5.

Material	E_g / eV (nm)	E_g / eV (nm)
White Nb_2O_5	3.20 (387)	2.44 (508)
Grey Nb_2O_5	3.16 (392)	2.39 (519)
Type of transition	direct (allowed)	indirect (allowed)

Here direct (allowed) and indirect (allowed) transitions are assumed and for both materials TiO_2 and Nb_2O_5, and the vacuum annealing treatment can be seen to lower the optical band gap for both types of transition (more pronounced for TiO_2). Additionally, the existence of indirect (allowed) electronic transition for these materials might be an indication of presence of defects.

The optical band gap (E_g) was estimated by UV-Vis spectroscopy in the diffuse reflectance mode and the following equations [63] were applied to analyse data: $\alpha = F(R) = \frac{(1-R)^2}{2R}$ and $(\alpha h v)^n = A(h v - E_g)$. Here $F(R)$ is the Kubelka-Munk function, R is the absolute reflectance to a given value of $h v$, α is the absorption coefficient, h is the Planck constant and v is the frequency. The parameter n is 2 or 2/3 for allowed and forbidden

direct transition, respectively; and 1/2 or 1/3 for allowed and forbidden indirect transition, respectively. Here allowed and direct transitions are assumed and for both materials TiO_2 and Nb_2O_5 the vacuum annealing treatment can be seen to lower the optical band gap.

4.2. Photoelectrochemical Characterization of Thin Films of White and Grey TiO₂

Photoelectrochemical data for white and grey TiO_2 films immersed in 1 M KOH in the dark and illuminated with 450 nm light are shown in Figure 6. The vacuum annealing treatment can be seen to result in (A) a considerable increase in capacitive current response (possibly due to enhanced electrical conductivity) and (B) a much lower photo-electrochemical response when exposed to blue light pulses.
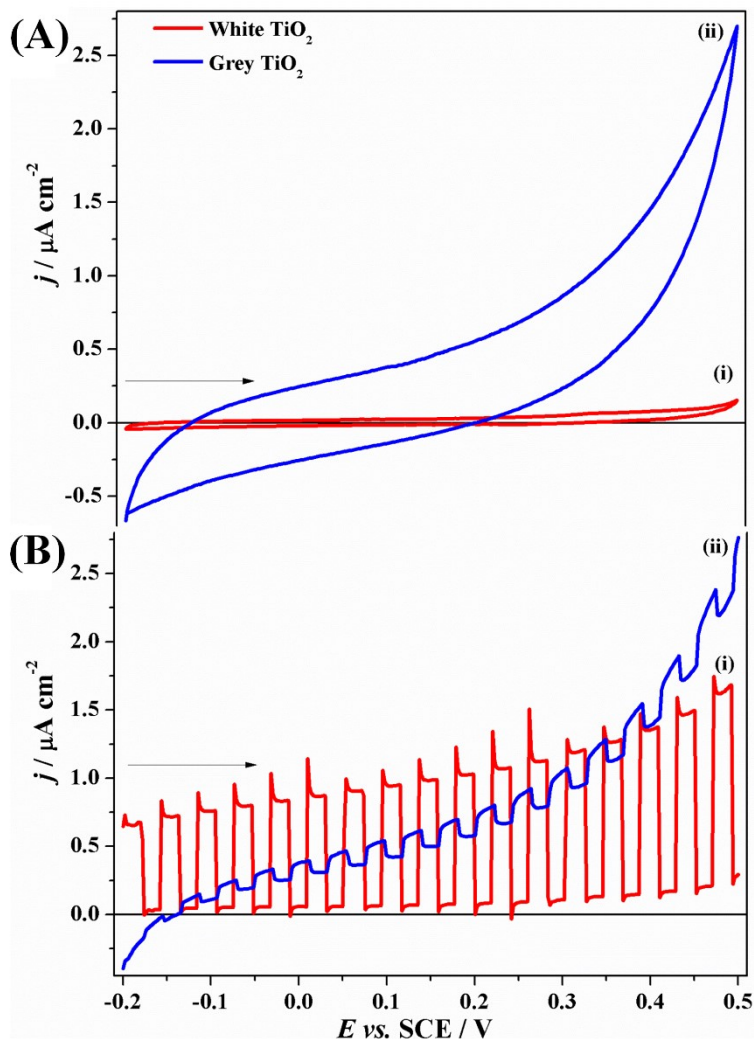
Figure 6. (A) Cyclic voltammograms (scan rate 20 mVs^{-1}) for (i) white and (ii) grey TiO$_2$ films immersed in 1 M KOH (pH 13.7). (B) Pulsed light linear sweep voltammogram (20 mVs^{-1}; $\lambda = 450$ nm, 1 s pulse time, nominally 100 mWcm^{-2}) for (i) white and (ii) grey TiO$_2$.

Figure 7 shows linear sweep voltammetry data for white (A) and grey (B) TiO$_2$ immersed in aqueous 1 M KOH and at $\lambda = 385$ nm. This wave length corresponds to an energy of 3.2 eV (in contrast to $\lambda = 450$ nm corresponding to 2.8 eV, see Figure 4) and is therefore more within the region of the band gap (in contrast to $\lambda = 450$ nm below the band gap). Photo-current responses are therefore significantly increased (compare Figure 7A to 6B). The

effect of the light intensity (going from 10% to 90%) on photo-current can be seen to be essentially linear, suggesting that the behavior of these films may be dominated by "photo-capacitance". This is the case for both, $\lambda = 385$ nm (Figure 7A) and $\lambda = 450$ nm (Figure 8A), which may suggest that there is no significant change in chemistry when changing wave length in this range (sub-band gap to super-band gap). Data in Figure 7B show photo transients for the vacuum annealed grey TiO_2 with significantly decreased responses. The plots in Figure 7C summarize the data for $\lambda = 385$ nm and in Figure 7D for $\lambda = 450$ nm. Trends are very similar and in both cases the vacuum annealing treatment causes an order of magnitude loss in photo currents.

A further result apparent from these plots is the essentially insignificant effect of front *versus* back illumination. Data here are essentially free of concentration gradient effects from light adsorption, but therefore also a significant amount of light (> 90%) passes through the samples without causing charge carrier formation. That is, photo-currents also remain relatively low. The variation of light intensity from 10% to 90% results in a close to linear correlation with photo-currents (Figure 7C and 7D) suggesting that "photo-capacitive" characteristics are important (see also decaying transients).
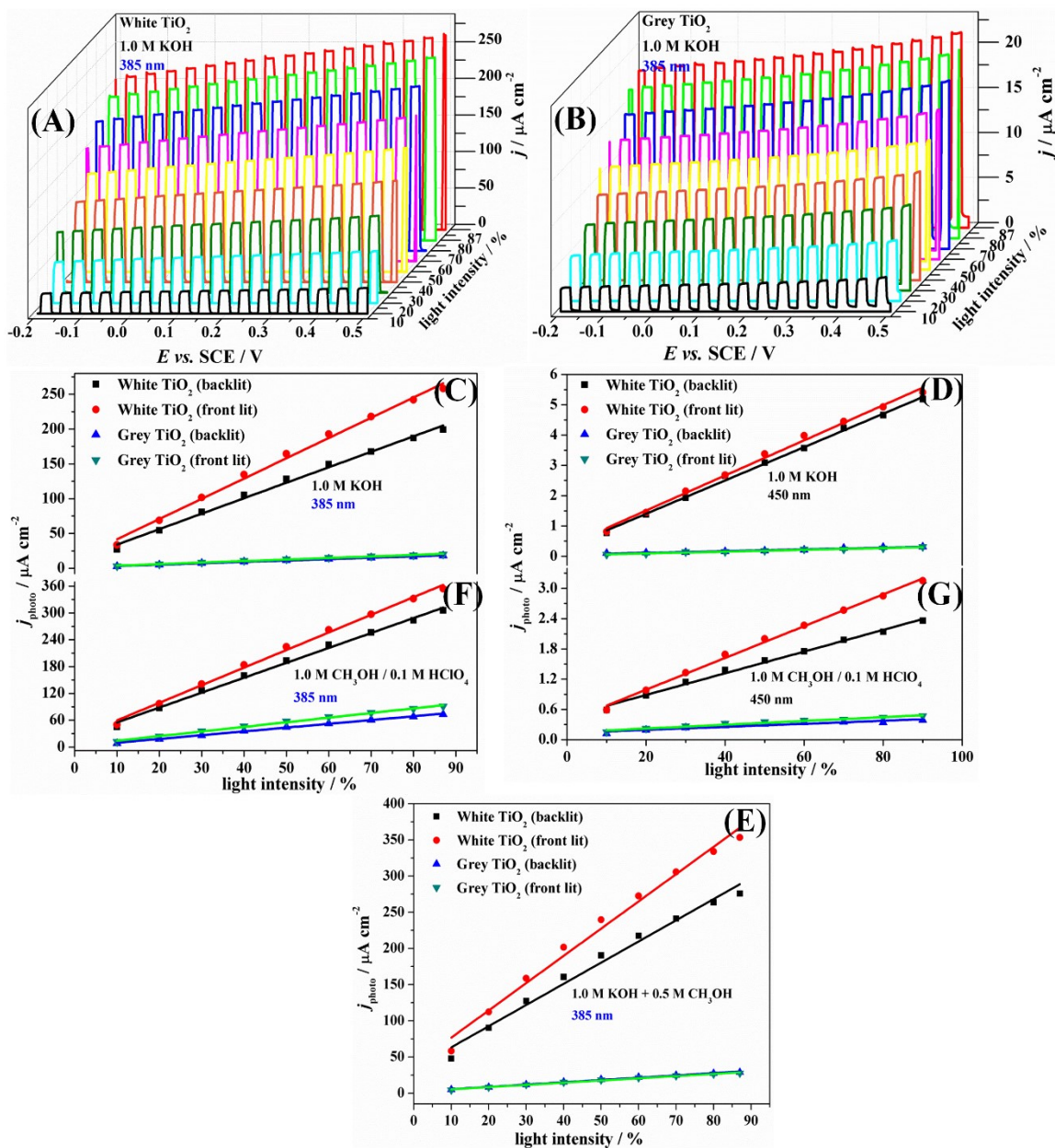
Figure 7. (A,B) Pulsed light linear sweep voltammograms (scan rate 20 mVs^{-1}; 1 s pulse time; $\lambda = 385$ nm; nominally 100 mWcm^{-2}) for white TiO$_2$ (A) and grey TiO$_2$ (B) immersed in 1 M KOH. Also shown are plots of photocurrent at 0.4 V vs. SCE *versus* light intensity for (C) front/back illumination for white/grey TiO$_2$ with $\lambda = 385$ nm in 1 M KOH, (D) front/back illumination for white/grey TiO$_2$ with $\lambda = 450$ nm in 1 M KOH, (E) front/back illumination for white/grey TiO$_2$ with $\lambda = 385$ nm in 1 M KOH/0.51 M CH$_3$OH, (F) front/back illumination for white/grey TiO$_2$ with $\lambda = 385$ nm in 0.1 M HClO$_4$/1 M CH$_3$OH, (G) front/back illumination for white/grey TiO$_2$ with $\lambda = 450$ nm in 0.1 M HClO$_4$/1 M CH$_3$OH.

24

The effect of adding a quencher (0.5 M CH_3OH) into the 1 M KOH is significant but limited to a 40% increase in photo currents (compare Figures 7C and 7E). Perhaps surprisingly, a very similar photo current effect is also seen in 0.1 M $HClO_4$ containing 1 M CH_3OH (Figure 7F and 7G). The similarity observed in these photo current responses may suggest that the surface chemistry at the TiO_2 | aqueous electrolyte interface (either alkaline or acidic pH) is not important and that instead bulk processes such as hole transport (or hole transfer to the surface [64]) could be rate limiting. This will be discussed in more detail below when exploring the effect of applied potential.

Figures 8A and 8B show photo transient data for $\lambda = 450$ nm (see plot in Figure 7D). The shape of photo transients remains very similar, although vacuum annealing clearly decreases the photo current responses. Trends for sub-band gap illumination agree well with super-band gap illumination. In the presence of 0.5 M CH_3OH (in 1 M KOH, Figure 8C and 8D) a change in transient shape is observed with a slower rise time for the vacuum annealed samples. However, consistently the vacuum annealed samples produced photo-currents an order of magnitude lower compared to those observed for air annealed samples.

From the data, there is very little evidence for surface chemistry to affect the photo currents. Effects caused by the vacuum annealing process are therefore also unlikely to be linked to surface processes and more likely to be associated with bulk recombination losses. These could be linked in turn to the electron mobility (or D_e) as recombination processes are likely to be diffusion limited. Zhang and coworkers [60] reported decreasing of photo currents ascribed to the formation of too many oxygen vacancies, which could act as electron and

25

hole recombination sites. Tian and coworkers [61] have also reported a decrease of photo current density for a reduction treatment at 500 °C to obtain the black TiO_2. Additionally, the authors stated that such higher reduction temperature would have caused the increase of the concentration of bulk oxygen vacancies, which acted as charge carrier traps for electron/hole recombination and resulting, consequently, in the decrease of the photocatalytic efficiency [61]. The decrease of photo current density values for the grey TiO_2 in this work might be linked to the vacuum annealing temperature. Such temperature treatment may result in excessive bulk doping with oxygen vacancies. We can also infer from Raman spectra and XRD data that the harsh vacuum treatment reduced the degree of crystallinity, which may affect detrimentally the photo-electrocatalytic performance of the material.
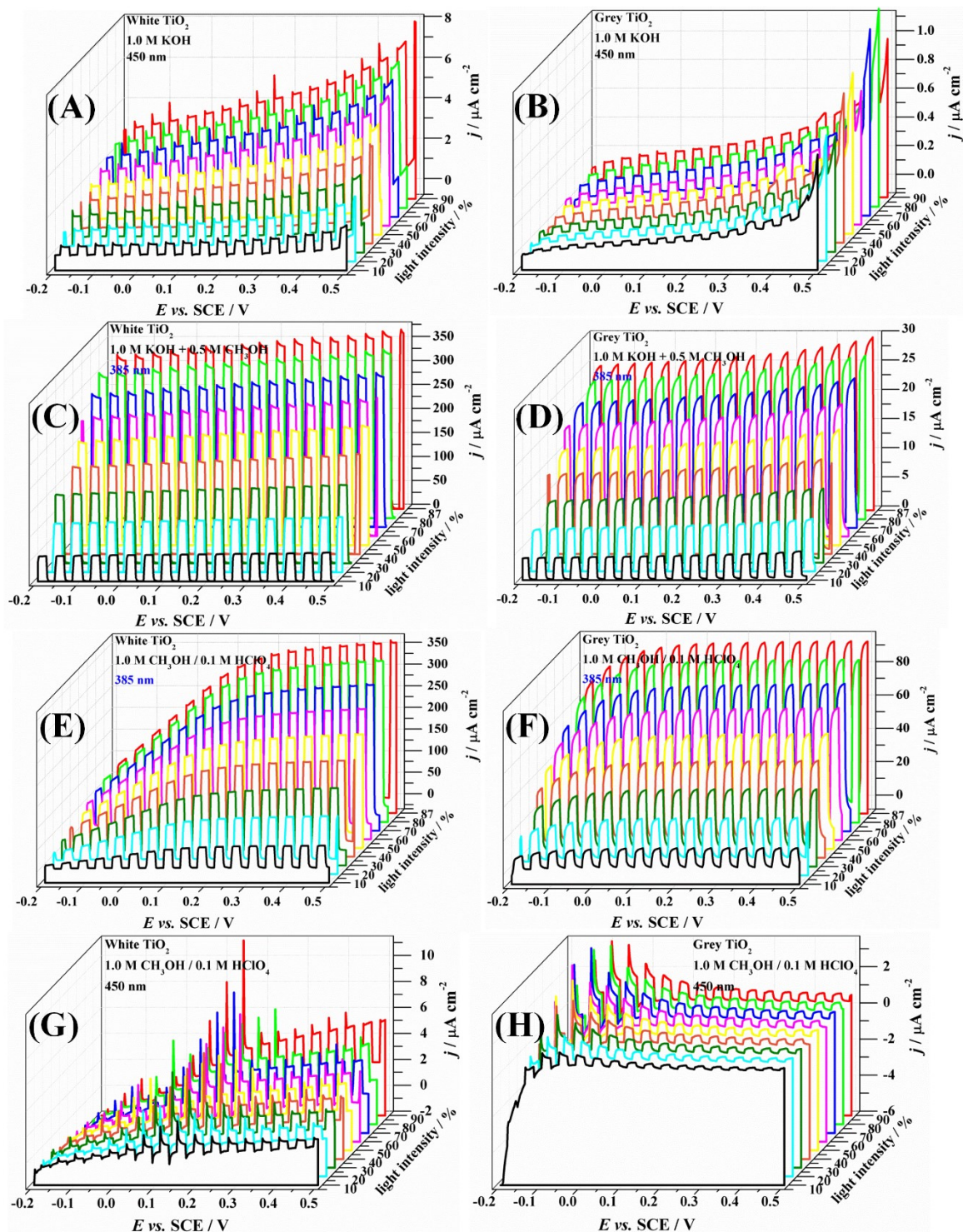
Figure 8. Linear sweep voltammograms (scan rate 20 mVs^{-1}; 1s light pulses; nominally 100 mWcm^{-2}; front illumination) for a TiO$_2$ film electrode (A) at λ = 450 nm for air annealed TiO$_2$ in 1 M KOH, (B) at λ = 450 nm for vacuum annealed TiO$_2$ in 1 M KOH, (C) at λ = 385 nm for air annealed TiO$_2$ in 1 M KOH + 0.5 M CH$_3$OH, (D) at λ = 385 nm for vacuum annealed TiO$_2$ in 1 M KOH + 0.5 M CH$_3$OH, (E) at λ = 385 nm for air annealed

TiO$_2$ in 0.1 M HClO$_4$ + 1 M CH$_3$OH, (F) at λ = 385 nm for vacuum annealed TiO$_2$ in 0.1 M HClO$_4$ + 1 M CH$_3$OH, (G) at λ = 450 nm for air annealed TiO$_2$ in 0.1 M HClO$_4$ + 1 M CH$_3$OH, and (H) at λ = 450 nm for vacuum annealed TiO$_2$ in 0.1 M HClO$_4$ + 1 M CH$_3$OH.

Data in Figure 8E and 8F show photo transients for 1 M CH$_3$OH in aqueous 0.1 M HClO$_4$ (see also plots in Figure 7F). With vacuum annealing photo currents are significantly lower and a difference in transient shape is observed. The corresponding data plots in Figure 7F and 7G suggest close to linear correlation of photo-current to light intensity and therefore dominating "photo-capacitive" transient characteristics in both cases. Again, an increase in k_{rec} upon vacuum annealing could be the underlying cause.

The effect of applied potential on photo current transients can be observed clearly when the pH of the aqueous solution is varied. A comparison of data in Figure 8C and 8E shows that a change in pH from 1 M KOH (pH = 13.7) to 0.1 M HClO$_4$ (pH = 1) causes a significant shift in the onset potential for photo currents but almost no change in the maximum photo current plateau. The onset of photo currents in 0.1 M HClO$_4$ can be estimated as approximately -0.3 V vs. SCE, whereas for 1 M KOH this value is significantly more negative (approximately ΔpH $\times$ 0.059 V = 0.75 V more negative due to surface equilibria). The gradual increase in photo current with applied potential is associated with diffusional extraction (and some migrational extraction) of electrons from the oxide film. For mesoporous oxides shielding effects from the surrounding electrolyte can suppress migrational transport to some extent, but the gradual increase of photo-currents with potential in Figure 7E suggests some contributions from migration. Due to oxide films being very thin in experiments reported here, it is likely that the plateau in the photo current transient is linked to successful extraction throughout the film. A further

increase in applied voltage beyond the plateau potential does not increase the photo-current and therefore does not affect the overall reaction. The observation that the surface conditions or solution pH do not significantly affect the maximum photo-current may be linked to the fact that all holes reaching the oxide surface are successfully consumed in the oxidation of methanol (or in the competing oxygen evolution reaction). The rate constant k_c is therefore likely to be "hole diffusion controlled" and not a true surface chemical rate constant. When equating the "grain size" of typically 1 nm (assumed) to the reaction layer for holes, $\delta_{reaction,h} = \sqrt{D_h/k_c}$, the rate constant is $k_c = 10^{-19}/(10^{-9})^2 = 0.1$ s^{-1}. Therefore k_c would have to be lower than 0.1 s^{-1} for hole transport to be sufficiently fast (to reflect a true chemical rate constant). Finally, for $\lambda = 450$ nm and in 0.1 M HClO$_4$ with 1 M CH$_3$OH (see Figure 8G and 8H) a reversible "photo-capacitive" potential range is observed for both white (at 0.1 V vs. SCE) and grey TiO$_2$ (at -0.1 V vs. SCE) films.

4.3. Photoelectrochemical Characterization of Thin Films of White and Grey Nb$_2$O$_5$

For thin films of Nb$_2$O$_5$ the vacuum annealing treatment causes grey coloration (see Figure 2) indicative of significant levels of oxygen vacancies being formed. Cyclic voltammetry of the films immersed into 1 M KOH (Figure 9A) confirms some minor increase in current probably linked to enhanced conductivity. When examining the photo-transient responses (Figure 9B; $\lambda = 450$ nm) clearly the vacuum annealed materials exhibits improved performance.
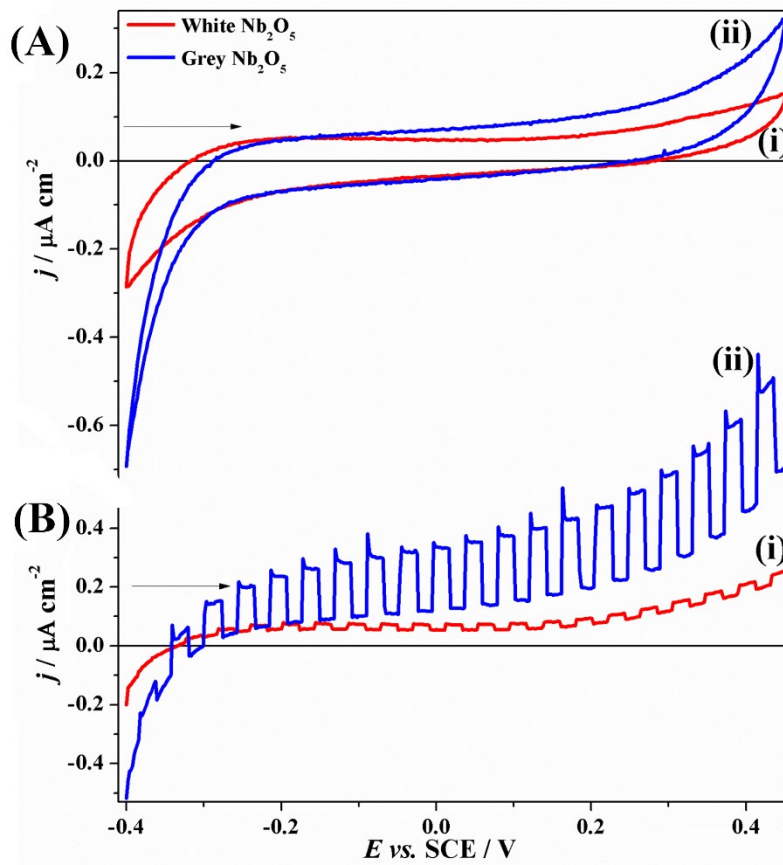
Figure 9. (A) Cyclic voltammograms (scan rate 20 mVs^{-1}) for (i) white and (ii) grey Nb$_2$O$_5$ films immersed in 1 M KOH. (B) Pulsed light linear sweep voltammogram (20 mVs^{-1}; $\lambda =$ 450 nm, 1 s pulse time, nominally 100 mWcm^{-2}) for (i) white and (ii) grey Nb$_2$O$_5$.

When changing the wave length to $\lambda = 385$ nm an increase in photo responses is observed (Figure 10A and 10B) according to the change in adsorption coefficient (see Figure 5). The variation in light intensity again gives rise to linear plots for photo-currents *versus* intensity. Plots in Figures 10C and 10D for $\lambda = 385$ nm and $\lambda = 450$ nm, respectively, show that there is no significant change (apart from a 10-fold increase in current due to a higher absorption at 385 nm) in the photochemical process for white Nb$_2$O$_5$ when changing the

30

wave length. Vacuum annealing is in all cases observed to improve photocurrents and there is only a minor deviation in data for grey Nb_2O_5 with back illumination. (Note the unusual difference in back and front illumination in data in Figure 10D. This could be linked to spurious processes that become apparent only at $\lambda = 450$ nm and at lower light intensity.) The addition of quencher (0.5 M CH_3OH in 1 M KOH) can be seen to increase photocurrents by a factor 3 for both air annealed and vacuum annealed samples, which is a strong sign for some additional hole reactivity at the surface without doping affecting the process. In this case the annealing process appears to affect primarily internal conductivity or recombination processes. This conclusion is further underpinned by the data observed in 0.1 M $HClO_4$ with 1 M CH_3OH (compare Figure 10F and 10E) where essentially the same trends are seen. In Figure 10G data for 0.1 M $HClO_4$ with 1 M CH_3OH are shown for $\lambda = 450$ nm. Perhaps interestingly, in this case (as well as to some extent in Figure 10F for $\lambda = 385$ nm) non-linearity in the photo-current versus light intensity plot is seen for the grey Nb_2O_5. This could be a sign of a dominating "photo-reactive" character of the transients (rather than "photo-capacitive"). This can be confirmed when exploring the shape of photo-transients in more detail.
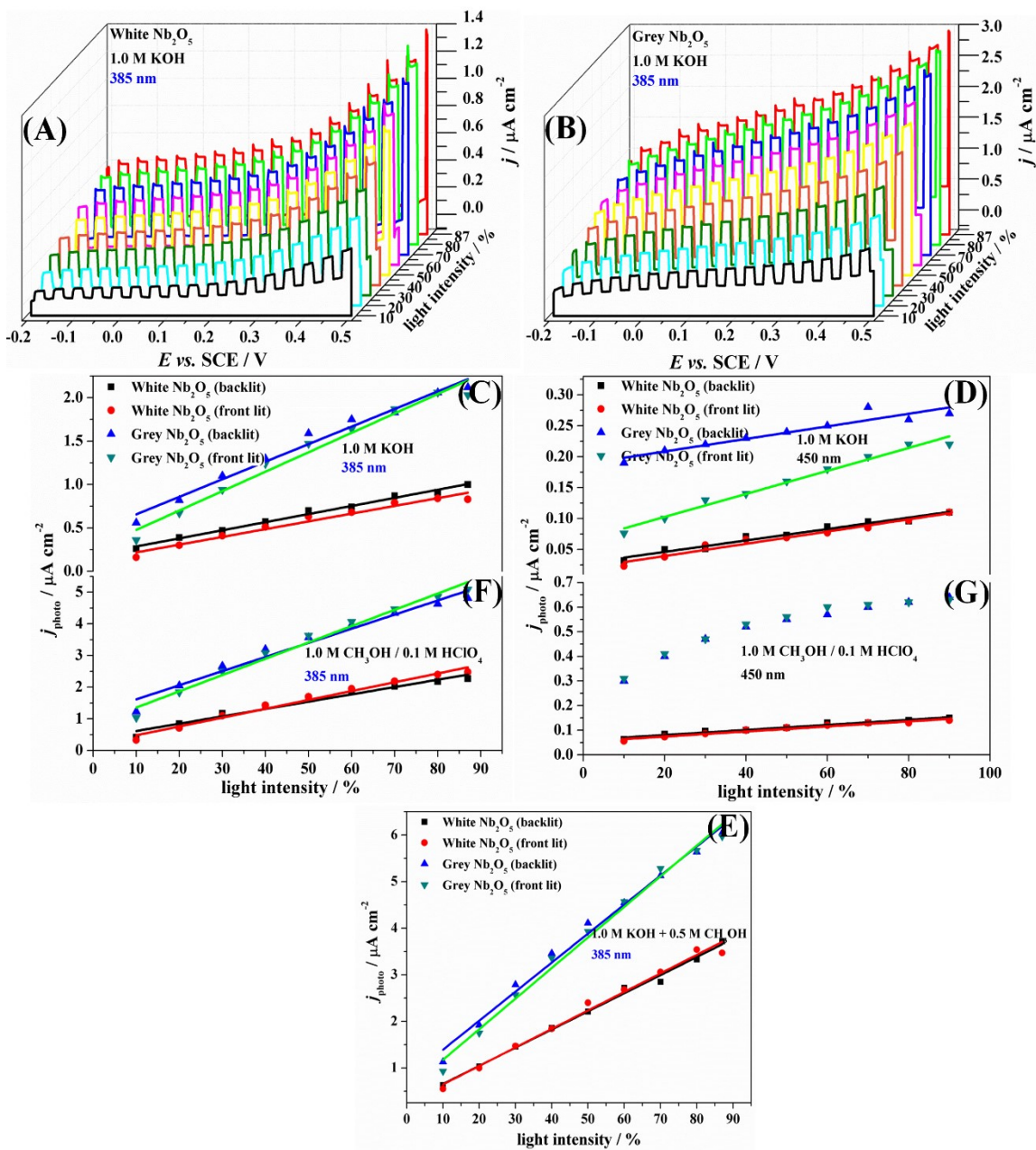
Figure 10. (A,B) Pulsed light linear sweep voltammograms (scan rate 20 mVs^{-1}; 1 s pulse time; λ = 385 nm; nominally 100 mWcm^{-2}) for white Nb_2O_5 (A) and grey Nb_2O_5 (B) in 1 M KOH. Also shown are plots of photocurrent at 0.4 V vs. SCE *versus* light intensity for (C) front/back illumination for white/grey Nb_2O_5 with λ = 385 nm in 1 M KOH, (D) front/back illumination for white/grey Nb_2O_5 with λ = 450 nm in 1 M KOH, (E) front/back illumination for white/grey Nb_2O_5 with λ = 385 nm in 1 M KOH/0.5 M CH_3OH, (F) front/back illumination for white/grey Nb_2O_5 with λ = 385 nm in 0.1 M $HClO_4$/1 M CH_3OH, (G) front/back illumination for white/grey Nb_2O_5 with λ = 450 nm in 0.1 M $HClO_4$/1 M CH_3OH.

Figures 11A and 11B show data for photo transients over a range of applied potentials. For $\lambda = 450$ nm both white and grey Nb_2O_5 show similar transient shapes indicative of fast electron extraction into the substrate and "photo-capacitive" conditions. When methanol is added as quencher, photo-transients increase and the transient shape changes more into a square (see Figures 11C and 11D). In 0.1 M $HClO_4$ with 1 M CH_3OH a shift in the onset of photocurrents is seen (due to the pH) but also a change in transient shape occurs (see particularly Figure 11E) indicative of more "photo-reactive" character. The vacuum annealed samples show significantly better defined more square shaped responses at both $\lambda = 450$ and $\lambda = 385$ nm with a more "photo-capacitive" character. The vacuum annealed grey Nb_2O_5 samples also exhibit a clear reversible "photo-capacitive" potential region from approximately -0.2 to 0.0 V vs. SCE (compare Figure 11H and 11G) possibly linked to a higher D_e (conductivity) allowing electrons to flow in and out of the film into states that are less reactive.
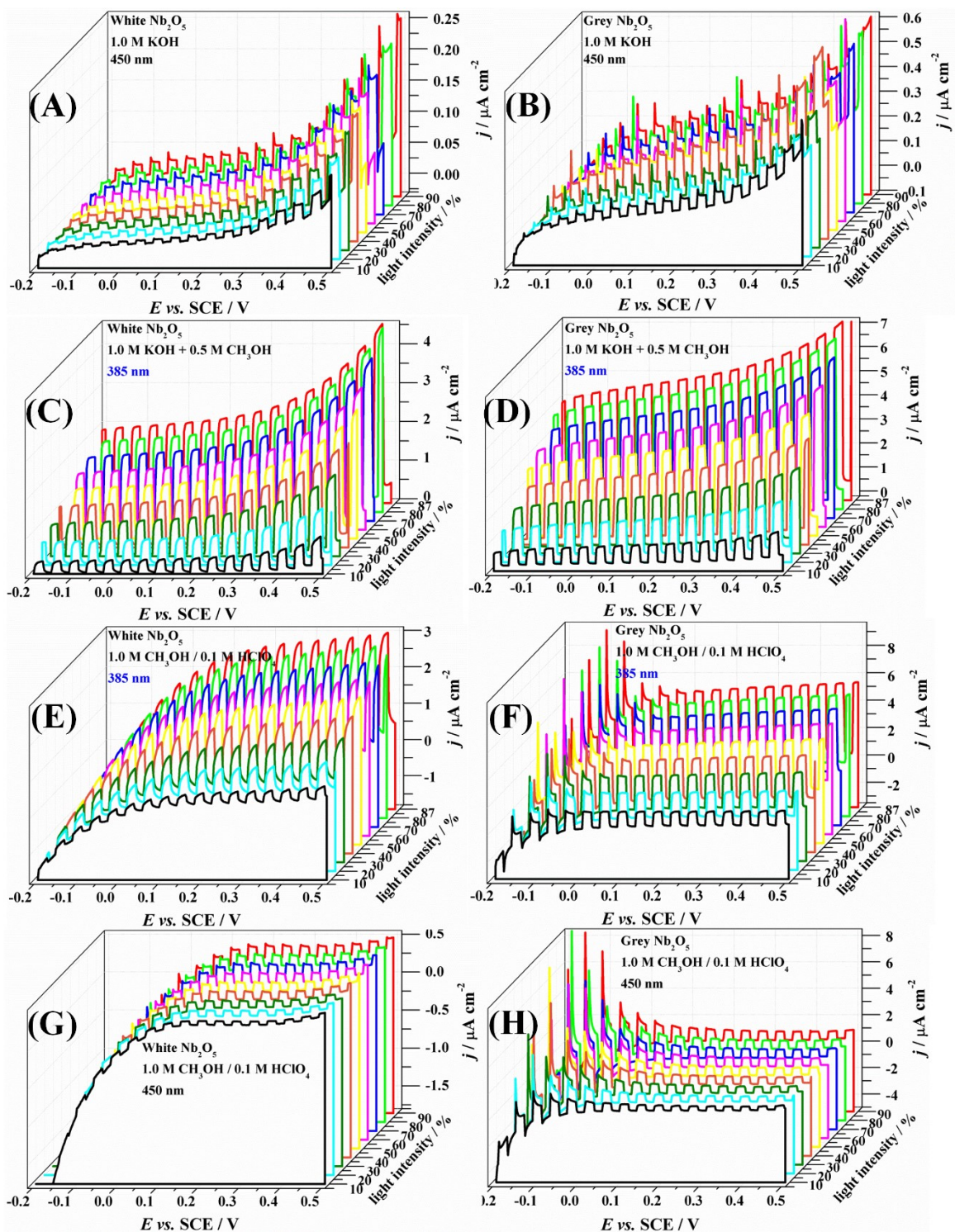
Figure 11. Linear sweep voltammograms (scan rate 20 mVs^{-1}; 1s light pulses; nominally 100 mWcm^{-2}; front illumination) for a Nb$_2$O$_5$ film electrode (A) at λ = 450 nm for air annealed Nb$_2$O$_5$ in 1 M KOH, (B) at λ = 450 nm for vacuum annealed Nb$_2$O$_5$ in 1 M KOH, (C) at λ = 385 nm for air annealed Nb$_2$O$_5$ in 1 M KOH/0.5 M CH$_3$OH, (D) at λ = 385 nm for vacuum annealed Nb$_2$O$_5$ in 1 M KOH/0.5 M CH$_3$OH, (E) at λ = 385 nm for air annealed

Nb$_2$O$_5$ in 0.1 M HClO$_4$/1 M CH$_3$OH, (F) at λ = 385 nm for vacuum annealed Nb$_2$O$_5$ in 0.1 M HClO$_4$/1 M CH$_3$OH, (G) at λ = 450 nm for air annealed Nb$_2$O$_5$ in 0.1 M HClO$_4$/1 M CH$_3$OH, and (H) at λ = 450 nm for vacuum annealed Nb$_2$O$_5$ in 0.1 M HClO$_4$/1 M CH$_3$OH.

4.4. Contrasting Behaviour of White and Grey TiO$_2$ and Nb$_2$O$_5$

At qualitative level, upon vacuum annealing TiO$_2$ exhibited a loss of photo-activity while Nb$_2$O$_5$ clearly exhibited improved photo-reactivity. The latter is consistent with literature reports and the former may be linked to over-doping [65]. Both materials showed increased photo-currents in the presence of quencher (due to holes being extracted faster) but both materials also exhibited the same photo-current plateaus in alkaline and acidic media indicative of a rate limiting process other than that linked to surface chemistry (*e.g.* hole transfer control rather than chemical reaction control). Details of the surface chemistry and the nature of products being formed have not been resolved, and therefore a range of processes are possible including both oxidation and reduction processes (*e.g.* water or perchlorate reduction). The effects of methanol quencher appeared to be similar for white and for grey oxide films. Most likely in this case appears to be that the rate limiting process is transport of holes towards/across the oxide surface (in the presence of quencher and with sufficiently positive potential applied in the plateau region). The effect of vacuum annealing seems to be linked mainly to electron mobility (or D_e). An increase in D_e should increase photo-currents (as in Nb$_2$O$_5$), but with increased doping levels may as well detrimentally affect the rate constant for recombination, k_{rec}, as this may be partially diffusion controlled. That is, higher doping levels can reduce the photo-currents.

The shape of photo-current transients (as well as the diagnostic photocurrent – light intensity behaviour) has been discussed in terms of "photo-capacitive" and "photo-reactive" contributions mainly linked to the presence of current transients that are decaying or rising, respectively. This implies that photo-currents alone are not a good indicator for water splitting activity. The time domain needs to be taken into account. In particular for Nb_2O_5 annealed in air (photo-reactive) and annealed under vacuum (photo-capacitive) the change in both current magnitude and in character appear significant. Photo-transients may provide information about both, (at longer times) the formation of products in the photo-electrochemical reaction and (at least initially) charging without production of products. More work will be required to distinguish photo-capacitive from photo-reactive processes and to follow the switch from the first to the second with time.

In future, the net charging of thin oxide films according to hole or electron excess concentrations when measured as a function of time (for example by Kelvin probe [66] or by scanning ion-conductivity microscopy or SICM [67]), could provide an additional experimental tool to explore the local kinetic and transport processes. A better understanding of concentration profiles and reaction rates in semiconductor film electrodes will allow more effective device architectures and processes to be developed.

5. Conclusions

It has been shown (based on a simple diffusion-reaction model) that thin oxide films (TiO_2 and Nb_2O_5) give photo-current transient data that are associated with initially "photo-capacitive" and later on with "photo-reactive" behaviour. Both, photo-capacitive and

photo-reactive behaviour, can be exploited in energy harvesting [68] and water splitting devices, respectively. A simplistic computational diffusion model is employed to explore charge carrier (holes and electrons) concentration gradients as they develop with time. Regions of excess charge carriers have been identified with close to the substrate electrode excess of net positive charge (due to rapid extraction of electrons) and close to the oxide | solution interface excess of net negative charge (due to reaction of holes). When compared to experimental data, the qualitative computational model is able to explain (i) the linearly light intensity dependent photo-current transients and (ii) the shape of photo-current transients. Photo-reactivity (associated with rate constant k_c) was shown to be enhanced by methanol quencher, but the ultimately (in the photocurrent plateau region) limited by interfacial hole transfer rather than by surface chemical reaction steps. Hole transfer and mobility (as well as electron mobility) need to be considered as important parameters in the overall reaction.

The vacuum-annealing process has been shown to significantly alter oxide photo-reactivity with grey TiO_2 being detrimentally affected and grey Nb_2O_5 being beneficially affected. Enhanced electron mobility is likely to be important in both cases. For TiO_2 it is suggested that the rate of electron transport (associated with D_e) is enhanced so much that it impacts on the rate of bulk recombination (as this may be diffusion controlled). In future, more work will be needed to link experimental data to computational analysis in a more quantitative manner and also to better the understanding at the atomistic level.

References

[1]   J.J. Qi, J.W. Chen, W.L. Meng, X.Y. Wu, C.W. Liu, W.J. Yue, M.T. Wang, Synth. Metals 222 (2016) 42–65.

[2]   A. Malviya, P.P. Solanki, Renew. Sustain. Energy Rev. 59 (2016) 662–691.

[3]   A.K. Jana, J. Photochem. Photobiol. A-Chem. 132 (2000) 1–17.

[4]   S.Y. Tee, K.Y. Win, W.S. Teo, L.D. Koh, S.H. Liu, C.P. Teng, M.Y. Han, Adv. Sci. 4 (2017) 1600337.

[5]   Y.X. Xu, A.L. Li, T.T. Yao, C.T. Ma, X.W. Zhang, J.H. Shah, H.X. Han, ChemSusChem 10 (2017) 4277–4305.

[6]   A. Nikokavoura, C. Trapalis, Appl. Surf. Sci. 391 (2017) 149–174.

[7]   K. Sivula, R. van de Krol, Nature Rev. Mater. 1 (2016) 15010.

[8]   J.Z. Su, L. Vayssieres, ACS Energy Lett. 1 (2016) 121–135.

[9]   W.J. Ong, L.L. Tan, Y.H. Ng, S.T. Yong, S.P. Chai, Chem. Rev. 116 (2016) 7159–7329.

[10]   W.G. Tu, Y. Zhou, Z.G. Zou, Adv. Mater. 26 (2014) 4607–4626.

[11]   R. Beranek, H. Kisch, Photochem. Photobiol. Sci. 7 (2008) 40–48.

[12]   J. Moir, N. Soheilnia, K. Liao, P. O'Brien, Y. Tian, K.S. Burch, G.A. Ozin, ChemSusChem 8 (2015) 1557–1567.

[13]   C.Q. Zhu, C.L. Li, M.J. Zheng, J.J. Delaunay, ACS Appl. Mater. Interfaces 7 (2015) 22355–22363.

[14]   T.Y. Yang, H.Y. Kang, U. Sim, Y.J. Lee, J.H. Lee, B. Koo, K.T. Nam, Y.C. Joo, Phys. Chem. Chem. Phys. 15 (2013) 2117–2124.

[15]   M.F. Gromboni, D. Coelho, L.H. Mascaro, A. Pockett, F. Marken, Appl. Catal. B-Environm, 200 (2017) 133–140.

[16]   J.Y. Zheng, S.I. Son, T.K. Van, Y.S. Kang, RSC Adv. 5 (2015) 36307–36314.

[17]   J.Y. Zheng, G. Song, C.W. Kim, Y.S. Kang, Nanoscale 5 (2013) 5279–5282.

[18]   J.Y. Zheng, G. Song, J.S. Hong, T.K. Van, A.U. Pawar, D.Y. Kim, C.W. Kim, Z. Haider, Y.S. Kang, Cryst. Growth Design 14 (2014) 6057–6066.

[19]   J.Y. Zheng, A.U. Pawar, C.W. Kim, Y.J. Kim, Y.S. Kang, Appl. Catal. B Environ. 233 (2018) 88–98.

[20]   J.Y. Zheng, A.P. Jadhav, G. Song, C.W. Kim, Y.S. Kang, Thin Solid Films 524 (2012) 50–56.

[21]   J.Y. Zheng, Z. Haider, T.K. Van, A.U. Pawar, M.J. Kang, C.W. Kim, Y.S. Kang, CrystEngComm 17 (2015) 6070–6093.

[22]   S. Sinha, D.K. Nandi, S.H. Kim, J. Heo, Solar Energy Mater. Solar Cells 176 (2018) 49–68.

[23]   A. Fujishima, K. Honda, Nature 238 (1972) 37–41.

[24]   F. Diquarto S. Piazza, C. Sunseri, Phys. Chem. Chem. Phys. 91 (1987) 437–441.

[25]   N.N. Greenwood, A. Earnshaw, Chemistry of the Elements, Butterworth-Heinemann, London, 1997, p. 977.

[26]   H. Gerischer, J. Electroanal. Chem. 58 (1975) 263–274.

[27]   S. Ahmed, I.A.I. Hassan, H. Roy, F. Marken, J. Phys. Chem. C 117 (2013) 7005–7012.

[28]   P. Atkins, J. de Paula, Physical Chemistry, 10th ed., Oxford University Press, Oxford 2014, p. 810.

[29]   A.N. Bondarchuk, L.M. Peter, G.P. Kissling, E. Madrid, J.A. Aguilar-Martinez, Z. Rymansaib, P. Iravani, M. Gromboni, L.H. Mascaro, A. Walsh, F. Marken, Appl. Catal. B-Environm. 211 (2017) 289–295.

[30]   M. Baek, D. Kim, K. Yong, ACS Appl. Mater. Interfaces 9 (2017) 2317–2325.

[31]   L.L. Kazmerski, D.M. Racine, Thin Solid Films 30 (1975) L19–L22.

[32]   V.C. Anitha, A.N. Banerjee, S.W. Joo, J. Mater. Sci. 50 (2015) 7495–7536.

[33]   X.Y. Liu, G.L. Zhu, X. Wang, X.T. Yuan, T.Q. Lin, F.Q. Huang, Adv. Energy
         Mater. 6 (2016) 1600452.

[34]   H. Song, C.X. Li, Z.R. Lou, Z.Z. Ye, L.P. Zhu, ACS Sust. Chem. Engineer. 5
         (2017) 8982–8987.

[35]   J.J. Xu, Z.L. Tian, G.H. Yin, T.Q. Lin, F.Q. Huang, Dalton Trans. 46 (2017)
         1047–1051.

[36]   A. Lepcha, C. Maccato, A. Mettenborger, T. Andreu, L. Mayrhofer, M. Walter,
         S. Olthof, T.P. Ruoko, A. Klein, M. Moseler, K. Meerholz, J.R. Morante, D.
         Barreca, S. Mathur, J. Phys. Chem. C 119 (2015) 18835–18842.

[37]   X.Y. Deng, H.X. Zhang, R.N. Guo, Q.L. Ma, Y.Q. Cui, X.W. Cheng, M.Z. Xie,
         Q.F. Cheng, Separation Purification Technol. 192 (2018) 329–339.

[38]   X.Y. Xin, T. Xu, J. Yin, L. Wang, C.Y. Wang, Appl. Catal. B-Environm. 176
         (2015) 354–362.

[39]   M. Zimbone, G. Cacciato, R. Sanz, R. Carles, A. Gulino, V. Privitera, M.G.
         Grimaldi, Catal. Commun. 84 (2016) 11–15.

[40]   G.H. Yin, Q.Y. Bi, W. Zhao, J.J. Xu, T.Q. Lin, F.Q. Huang, ChemCatChem 9
         (2017) 4389–4396.

[41]   N. Liu, C. Schneider, D. Freitag, E.M. Zolnhofer, K. Meyer, P. Schmuki,
         Chem.-A Europ. J. 22 (2016) 13810–13814.

[42]   A. Hazra, S. Das, J. Kanungo, E. Bontempi, C.K. Sarkar, P. Bhattacharyya, S.
         Basu, J. Mater. Sci.-Mater. Electron. 24 (2013) 1658–1663.

[43]   C. Di Valentin, G. Pacchioni, A. Selloni, J. Phys. Chem. C 113 (2009) 20543–
         20552.

[44]   H. Yin, T.Q. Lin, C.Y. Yang, Z. Wang, G.L. Zhu, T. Xu, X.M. Xie, F.Q. Huang,
         M.H. Jiang, Chem.-A Europ. J. 19 (2013) 13313–13316.

[45]   C. Nico, T. Monteiro, M.P.F. Graca, Prog. Mater. Sci. 80 (2016) 1–37.

[46]   R.A. Rani, A.S. Zoolfakar, A.P. O'Mullane, M.W. Austin, K. Kalantar-Zadeh,
         J. Mater. Chem. A 2 (2014) 15683–15703.

[47]   H. Wen, Z.F. Liu, J. Wang, Q.B. Yang, Y.X. Li, J. Yu, Appl. Surf. Sci. 257
         (2011) 10084–10088.

[48]   R. Ghosh, M.K. Brennaman, T. Uher, M.R. Ok, E.T. Samulski, L.E. McNeil, T.J. Meyer, R. Lopez, ACS Appl. Mater. Interf. 3 (2011) 3929–3935.

[49]   R. Brayner, F. Bozon-Verduraz, Phys. Chem. Chem. Phys. 5 (2003) 1457–1466.

[50]   S. Heusing, D.L. Sun, J. Otero-Anaya, M.A. Aegerter, Thin Solid Films 502 (2006) 240–245.

[51]   X.Q. Ma, Y. Chen, H. Li, X.L. Cui, Y.H. Lin, Mater. Res. Bull. 66 (2015) 51–58.

[52]   H.L. Cui, G.L. Zhu, Y. Xie, W. Zhao, C.Y. Yang, T.Q. Lin, H. Gu, F.Q. Huang, J. Mater. Chem. A 3 (2015) 11830–11837.

[53]   W.L. Zhao, W. Zhao, G.L. Zhu, T.Q. Lin, F.F. Xu, F.Q. Huang, Dalton Trans. 45 (2016) 3888–3894.

[54]   J.S. Baik, G. Yun, M. Balamurugan, S.K. Lee, J.H. Kim, K.S. Ahn, S.H. Kang, J. Electrochem. Soc. 163 (2016) H1165–H1170.

[55]   A. Nowak, J. Persson, B. Schmelzer, J. Szade, K. Szot, J. Phys. D-Appl. Phys. 47 (2014) 135301.

[56]   L. Hao, K. Miyazawa, H. Yoshida, Y. Lu, Mater. Res. Bull. 97 (2018) 13–18.

[57]   L.M. Peter, E.A. Ponomarev, G. Franco, N.J. Shaw, Electrochim. Acta 45 (1999) 549–560.

[58]   R.G. Compton, E. Laborda, K.R. Ward, Understanding Voltammetry: Simulation of Electrode Processes, Imperial College Press, London, 2014, p. 9.

[59]   U.S. Department of Commerce National Bureau of Standards. Standard X-ray Diffraction Powder Patterns Monograph 25 – Section 7, 1969, p. 82.

[60]   L.K. Frevel, H.W. Rinn, Anal. Chem. 27 (1955) 1329–1330.

[61]   Z. Zhang, X. Tan, T. Yu, L. Jia, X. Huang, Int. J. Hydrogen Energ. 41 (2016) 11634–11643.

[62]   Z. Tian, H. Cui, G. Zhu, W. Zhao, J. Xuo, F. Shao, J. He, F. Huang, J. Power Sources. 325 (2016) 697–705.

[63]   F.W. Lucas, A.R.F. Lima, L.H. Mascaro, RSC Adv. 5 (2015) 18295–18299.

[64]   H.K. Dunn, J.M. Feckl, A. Müller, D. Fattakhova-Rohlfing, S.G. Morehead, J. Roos, L.M. Peter, C. Scheu, T. Bein, Phys. Chem. Chem. Phys. 16 (2014) 24610–24620.

[65]   G.M. Wang, Y.C. Ling, Y. Li, Nanoscale 4 (2012) 6682–6691.

[66]   W. Melitz, J. Shen, A.C. Kummel, S. Lee, Surf. Sci. Reports 66 (2011) 1–27.

[67]   C.C. Chen, Y. Zhou, L.A. Baker, Ann. Rev. Anal. Chem. 5 (2012) 207–228.

[68]   N.S. van Leeuwen, B. Blom, M.Y. Xie, V. Adamaki, C.R. Bowen, M.A. de Araújo, L.H. Mascaro, P.J. Cameron, F. Marken, ACS Appl. Energy Mater. 1 (2018) 38–42.